RSC Advances

PAPER

View Article Online
View Journal | View Issue

Cite this: *RSC Adv.*, 2020, **10**, 17660

Cobalt–carbon/silica nanocomposites prepared by pyrolysis of a cobalt 2,2′-bipyridine terephthalate complex for remediation of cationic dyes†

Nusaybah Alotaibi, [a] Hassan H. Hammud, *[a] Ranjith Kumar Karnati, [a] Syed Ghazanfar Hussain,[b] Javed Mazher[b] and Thirumurugan Prakasam [c]

Recently, carbon nanostructures have attracted interest because of their unique properties and interesting applications. Here, CoC@SiO_2-850 (**3**) and CoC@SiO_2-600 (**4**) cobalt–carbon/silica nanocomposites were prepared by solid-state pyrolysis of anthracene with Co(tph)(2,2′-bipy)·$4H_2O$ (**1**) complex in the presence of silica at 850 and 600 °C, respectively, where 2,2′-bipy is 2,2′-bipyridine and tph is the terephthalate dianion. Moreover, Co(μ-tph)(2,2′-bipy) (**2**) was isolated and its X-ray structure indicated that cobalt(II) has a distorted trigonal prismatic coordination geometry. **2** is a metal–organic framework consisting of one-dimensional zigzag chains within a porous grid network. **3** and **4** consist of cobalt(0)/cobalt oxide nanoparticles with a graphitic shell and carbon nanotubes embedded in the silica matrix. They were characterized by scanning electron microscopy (SEM), transmission electron microscopy (TEM), powder X-ray diffraction (XRD), Brunauer–Emmett–Teller (BET), Raman spectroscopy, and X-ray photoelectron spectroscopy (XPS). XPS revealed that the nanocomposites are functionalized with oxygen-containing groups, such as carboxylic acid groups. In addition, the presence of metallic cobalt nanoparticles embedded in graphitized carbon was verified by XRD and TEM. The efficiency of **3** for adsorption of crystal violet (CV) dye was investigated by batch and column experiments. At 25 °C, the Langmuir adsorption capacity of **3** for CV was 214.2 mg g^{-1} and the fixed-bed column capacity was 36.3 mg g^{-1}. The adsorption data were well fitted by the Freundlich isotherm and pseudo-second-order kinetic model. The adsorption process was spontaneous and endothermic.

Received 25th March 2020
Accepted 27th April 2020

DOI: 10.1039/d0ra02752a

rsc.li/rsc-advances

1. Introduction

Organic dyes are present in the wastewater of various industries, such as the textile, paint, and pigment industries. It has been reported that there are at least 100 000 commercially available dye types[1] and over 10 000 tons of dyes are manufactured per annum worldwide. It is assumed that 1–10% of the used dyes are discharged into wastewater.[2] Consequently, dyes are one of the main classes of water contaminants. They are harmful to aquatic life and human beings. Long-term exposure to dyes is considered to be a potential health hazard. They may cause skin irritation, respiratory problems, and cancer in humans.[3] Thus, effective removal of dyes from wastewater has become a major concern to protect human health. Various methodologies have been developed for removal of toxic dyes from wastewater. Examples are coagulation, oxidation, and biological treatment. However, these techniques either lack flexibility in design and operation or they are very sensitive to different parameters, which limits their efficiency for removal of toxic dyes. Adsorption has become one of the most popular techniques for water purification because of its high performance for having high efficiency of removing pollutants in short time, low cost of adsorbents materials and equipment, ease of operation since no sophisticated equipment is needed. The most common sorbent is activated carbon. However, activated carbon possesses some disadvantages, such as flammability, regeneration difficulties, and weak affinity for cationic and anionic dyes in aqueous solution,[4] which decrease its applicability for water treatment. Carbon nanostructures are relatively new sorbents that have some advantages over activated carbon adsorbents. They have been proven to be efficient for removal of different dyes from wastewater. They possess large surface area, high thermal and chemical stabilities,[5] and low mass density,[6] making them ideal candidates for adsorbents.

[a]*Department of Chemistry, College of Science, King Faisal University, Al-Ahsa 31982, Saudi Arabia. E-mail: hhammoud@kfu.edu.sa; Tel: +966 13 589 9579*

[b]*Department of Physics, College of Science, King Faisal University, Al-Ahsa 31982, Saudi Arabia*

[c]*Chemistry Program, New York University Abu Dhabi (NYUAD), Abu Dhabi, United Arab Emirates*

† Electronic supplementary information (ESI) available: Additional figures and tables and X-ray crystallographic data. CCDC 1966192 contains the supplementary crystallographic data for crystal (**2**) in this paper. For ESI and crystallographic data in CIF or other electronic format see DOI: 10.1039/d0ra02752a

Several techniques have been developed to prepare carbon nanostructures, including plasma or thermally enhanced chemical vapor deposition,[7] arc discharge,[8] and laser ablation.[9] However, these methods have several disadvantages making them inconvenient for both academic and industrial chemists. They require high energy and expensive instruments. The amount of nanocarbons produced is low and not sufficient for large scales application as column fillers in water treatment industries. Therefore, there is an urgent need to prepare well-developed crystalline graphitic nanostructures by low-cost synthetic procedures. In this respect, an alternative method is the pyrolytic synthesis of novel carbon nanostructures in large-scale from transition metal complex precursors. High reactivity of organometallic precursors in thermal pyrolysis, was reported by Vollhardt and co-workers in an early study.[10] They reported that mixing dehydrobenzoannulene (DBA) and $Co_2(CO)_8$ increases the reactivity of the organometallic compound through complexation of the alkyne groups. Carbonization of the obtained reactive complex required 200 °C lower compared to cobalt-free DBA. Furthermore, heating to higher temperature 800 °C for 6 h led to the formation of onions, multi-walled carbon nanotubes (CNTs), graphitic and amorphous carbon.[10,11] Therefore, solid-state pyrolysis of organometallic complexes under an inert atmosphere is an alternative method for preparing carbon nanostructures with a wide range of sizes and structures. It provides metal nanoparticle catalysts that enhance graphitization at relatively low temperature (catalytic graphitization), while decomposing organic ligand deposits on the metal catalyst to produce the desired carbon nanostructures. In addition, it can result in formation of functionalized metal–carbon nanocomposites, which are considered to be good candidates for dye removal. Furthermore, embedding metals into porous carbon can enhance the adsorption performance, which has recently attracted much interest.[12] It has been found that encapsulation of metal particles can circumvent diffusion resistance, promotes mass transfer,[13] and provides new properties, such as magnetism.[12] It may also create specific binding sites that enhance adsorption.[12,14] In addition, the adsorbent can be easily separated from aqueous solution after the adsorption process by applying an external magnetic field instead of centrifugation or filtration.[13]

Several metal–carbon nanocomposites for dye removal have been reported. For example, Fe_2O_3/nanoporous carbon showed a maximum adsorption capacity of 292.4 mg g^{-1} for methylene blue (MB).[15] Hammud *et al.*[16] also reported that cobalt–carbon nanocomposites derived from cobalt phenanthroline complex have an adsorption capacity of 492 mg g^{-1} for malachite green. Recently carbon-based adsorbents have been used by researchers for adsorption of crystal violet: Du *et al.*, Fe_3O_4–graphene–biochar composite;[17] Sellaoui *et al.*, multi-walled carbon nanotubes functionalized with hydroxyl and carboxylic acid groups;[18] Wang *et al.*, EDTA/graphene oxide functionalized corncob;[19] Hasan *et al.*, zirconia–carbon composite;[20] and Mohamed *et al.*, grafted sodium alginate/ZnO/graphene oxide composite.[21]

Herein, we report the synthesis of highly porous cobalt–carbon/silica nanocomposite CoC@SiO_2 by solid-state pyrolysis of Co(μ-tph)(2,2′-bipy)$(H_2O)_2 \cdot 2H_2O$ in presence of anthracene as an additional carbon source and silica as a supportive substrate. Where 2,2′-bipy is 2,2′-bipyridine and tph is the terephthalate ion. The two ligands were chosen because they provide porous metal–organic framework complexes with cobalt ion. 2,2′-Bipyridine ligand is carbon-rich and can increase the carbon conversion yield. In addition, it is a nitrogen-containing aromatic ligand, and it is expected to play an important role in synthesis of graphitized nitrogen-doped carbon. The oxygen-donor co-ligand tph was used because the bridging properties of the two *para* carboxylate groups enhance formation of metal–organic frameworks (MOFs) and supramolecular networks ranging from one-dimensional (1D) to three-dimensional (3D) structures. Thus, it can be used to construct complexes with pores, which is crucial for synthesis of derivatized porous carbon nanostructures. Furthermore, cobalt ions are less likely to be leached in weakly acidic solution because of their relatively high stability owing to the graphitic shell.[12] The cheap and abundant porous silica was used as substrate in order to provide easy to handle, abundant, stable and regenerable cobalt–carbon/silica nanocomposites CoC@SiO_2. Finally, crystal violet (CV) dye has adverse effects on aquatic and human life, including genotoxic and carcinogenic effects. Thus, we have investigated its removal from water by the CoC@SiO_2 nanocomposite.

2. Materials and methods

2.1 Materials

All of the chemicals were used as received without further purification. Cobalt(II) nitrate hexahydrate (99%, SDFCL), 1,10-phenanthroline (>99%, Acros Organics), terephthalic acid (>99%, Acros Organics), sodium hydroxide (pure, Acros Organics), ethanol (ACS grade, Scharlau), *N*,*N*-dimethylformamide (DMF, 99.9%, Panreact), CV (pure, Acros Organics), MB (pure, Acros Organics), and methyl orange (MO, pure, Acros Organics) were used in the experiments.

2.2 Synthesis of Co(tph)(2,2′-bipy)·$4H_2O$ (1)

Disodium terephthalate salt was prepared by a literature procedure.[22] Sodium hydroxide (2.76 g, 137.92 mmol) was dissolved in deionized water (10 mL). Terephthalic acid (3.46 g, 20.86 mmol) was added to the sodium solution and it was stirred at 60 °C. Deionized water was then slowly added up to 80 mL to completely dissolve the residue and ethanol was added to the solution at 90 °C until the solution produced a white precipitate. The reaction mixture was refluxed at 90 °C for 12 h, and the precipitate was then collected by filtration and dried at 150 °C for 1 h.

Co(tph)(2,2′-bipy)·$4H_2O$ complex (**1**) was prepared as follows.[23] 2,2′-Bipyridine (0.780 g, 5 mmol) was dissolved in absolute ethanol (20 mL) and mixed with an aqueous solution (200 mL) of $Co(NO_3)_2 \cdot 6H_2O$ (0.914 g, 5 mmol). An aqueous solution (75 mL) of disodium terephthalate (1.05 g, 5 mmol) was gradually added for 2 h under stirring. A light orange precipitate formed and the solution was left to stand overnight. The

precipitate was then filtered off, washed with water and ethanol, and left to dry in air, resulting in 0.835 g yield (55.96% based on cobalt). Analysis (%) calc. for $C_{20}H_{20}CoN_2O_8$: C, 47.91; H, 4.47; N, 6.21. Found: C, 48.35; H, 4.53; N, 6.0.

2.3 Synthesis of Co(μ-tph)(2,2′-bipy) (2)

Co(μ-tph)(2,2′-bipy) complex (**2**) was prepared as follows. Cobalt nitrate hexahydrate (0.291 g, 1 mmol) was dissolved in 5 mL of DMF, and then 5 mL of DMF was added to the cobalt solution. Subsequently, 2,2′-bipyridine (0.156 g, 1 mmol) and disodium terephthalate (0.166 g, 1 mmol) were dissolved in 7 mL of DMF and layered over the bilayer solution. After 2 months, red needle crystals suitable for X-ray analysis were obtained and collected.

2.4 Solid-state synthesis of the cobalt–carbon silica nanocomposites CoC@SiO_2-850 (3) and CoC@SiO_2-600 (4)

Co(tph)(2,2′-bipy)·$4H_2O$ (**1**) (0.5 g), anthracene (0.5 g), and silica (0.5 g) were mixed and placed in a crucible in a nitrogen gas furnace and heated at 300 °C for 2 h (intermediate stage) and then at 850 °C for 10 h (final stage). After slow cooling to room temperature, 0.554 g of CoC@SiO_2-850 (**3**) was obtained as a black powder. CoC@SiO_2-600 (**4**) (0.556 g) was obtained as a black powder by a similar procedure with an intermediate stage of 300 °C for 2 h and a final stage of 600 °C for 8 h. Treatment of **4** with 10% acid gave porous nanocomposite **5** with loss of some cobalt by dissolution.

2.5 Adsorption study

In all of adsorption experiments, a conical flask containing 50 mL of dye solution with an initial concentration $C_0 = 50, 100, 150, 200, 250$, or 300 mg L^{-1} and 0.05 g of CoC@SiO_2-850 adsorbent (**3**) was placed in a shaker at a rotation speed of 120 rpm. The concentration of dye remaining in solution C_e (mg L^{-1}) was obtained by recording the absorbance at λ_{max} with a ultraviolet-visible (UV-Vis) spectrophotometer (Shimadzu, UV-1800). λ_{max} was 582, 664, and 464 nm for CV, MB, and MO respectively. The amount of CV dye adsorbed at equilibrium (q_e, mg g^{-1}) was then calculated. A fixed-bed column study was performed using a column with 1 cm inner diameter and 22 cm height. The column was packed with 0.5 g adsorbent with glass wool in between. The bed height was about 1.5 cm. The dye solution with an initial concentration of 50 mg L^{-1} was then added into the column at a flow rate of 1 mL min^{-1}. Effluent aliquots were collected at specified intervals of time and their absorbance was recorded with a UV-Vis spectrophotometer at $\lambda_{max} = 582$ nm to determine the residual dye concentration. The column experiments were terminated when the column reached exhaustion. The column bed was regenerated with 0.5 M HCl. Column desorption was confirmed by UV-Vis spectrophotometry. The bed was then washed several time with deionized water until the pH of effluent remained constant at about 7.0. The column was then used for another cycle.

2.6 Characterization techniques

Morphological characterization was performed by field emission scanning electron microscopy (FE-SEM, QuantaFEG450, FEI, and JSM-6460LV). Transmission electron microscopy (TEM) images were obtained with a JEM-1011 transmission electron microscope (JEOL, Tokyo, Japan) operated at 80 kV. Powder X-ray Diffraction (XRD) was performed with an Inel Equinox 1000 powder diffractometer equipped with a CPS 180 detector (filtered Co $K\alpha_1$ irradiation, 30 kV, 30 mA, $\lambda = 1.789$ Å, zero background spinning sample holder). The powder patterns were analysed with Mass Crystal Impact software (version 1.11e) for phase identification, and both COD and ICSD databases were used. Raman spectra were recorded with a DXR Raman spectrometer (Thermo Scientific). X-ray photoelectron spectroscopy (XPS) measurements were performed with a SPECS GmbH high vacuum multi-technique surface analysis system equipped with a Mg Kα 1253.6 eV X-ray source. During data analysis, spectra from the surface were calibrated by setting the C 1s line to 284.8 eV. Quantification of the surface composition was obtained from the XPS peak intensities using relative sensitivity factors. Fourier transform infrared (FTIR) spectra were recorded with a Cary 630 FTIR spectrometer (Agilent). Elemental analysis (CHN) was performed with a PerkinElmer 2400 elemental analyser. Nitrogen adsorption measurements were performed with an adsorption apparatus (TriStar II Plus 2.02, Micromeritics). Adsorption isotherms were obtained at 77 K. A degassing process was performed before the measurements. The obtained data were analysed with Micro Active for Tri Star II Plus 2.02 software.

2.7 X-ray crystallography

The crystal data and collection details pertaining to single-crystal X-ray analysis of Co(μ-tph)(2,2′-bipy) (**2**) are given in Table S1.† The XRD data of complex **2** were collected using a Bruker APEX DUO diffractometer equipped with a Cobra cooling device (Oxford Cryosystems) with graphite-monochromated Mo Kα radiation ($\lambda = 0.71073$ Å) and a charge-coupled device as the area detector. Data collection, integration, scaling, and absorption correction were performed with Bruker Apex 3 software. Data reduction was performed using SAINT2 and XPREP. All of the data were corrected for Lorentzian, polarization, and absorption effects using the SADABS4 program. Structure determination and refinement using the OLEX2 interface was performed using the full matrix least-squares method based on F^2 against all reflections, as implemented in SHELXL2014/7.6. The hydrogen atoms bonded to carbon atoms were fixed using the HFIX command in SHELX-TL.

3. Results and discussion

3.1 Characterization of Co(tph)(2,2′-bipy)·$4H_2O$ (1)

3.1.1 FTIR spectroscopy. FTIR spectra of **1**, 2,2′-bipy, and Na_2tph are shown in (Fig. S1†), and the assignments of significant IR spectral bands of the ligands and **1** are given in (Table S2†). The positions of the C=N and C=C bands of the 2,2′-bipy[24] ligand shifted upon complexation, indicating involvement of nitrogen in coordination. In addition, absorption peaks assigned to aromatic C–H vibrations were observed in FTIR

spectrum of 1, suggesting coordination of 2,2′-bipy. The bands at 1551, 1381, 742, and 506 cm^{-1} corresponding to the COO^- vibrations of sodium terephthalate[25,26] shifted to 1533, 1371, 734, and 504 cm^{-1}. The blue shift was attributed to complexation with the cobalt ion. The coordination mode of terephthalate ion can be determined from the difference between $\nu_{sym}(COO^-)$ and $\nu_{asym}(COO^-)$ frequencies relative to the value of the free terephthalate ion (Δ).[27] The Δ value of cobalt complex was lower than that of sodium terephthalate, suggesting that the coordination mode was bidentate.[26] The broad band at about 3255 cm^{-1} indicated the presence of water molecules.

3.1.2 Thermogravimetric analysis. To optimize the pyrolysis temperature, thermogravimetric analysis (TGA) was performed. The TGA curve of cobalt complex **1** showed three stages of weight loss in the temperature range 35–800 °C (Fig. S2†). The first stage (~150 °C) exhibited weight loss of 15.8%, corresponding to the loss of four water molecules (calculated 15.96%). The sharp weight loss in the temperature range 279–375 °C (9.4%) may correspond to the loss of one CO_2 molecule from the terephthalate ion (calculated 9.2%).[28] The third stage of decomposition in the narrow temperature range 400–534 °C accompanied by a sharp exothermic peak occurred because of simultaneous loss of the second CO_2 molecule from the carboxylate group of the terephthalate ion and the 2,2′-bipyridine ligand (found 47.63%, calculated 44.36%).

3.2 X-ray structure of Co(μ-tph)(2,2′-bipy) (2)

The polymeric structure of Co(μ-tph)(2,2′-bipy) (**2**) is a 1D zigzag chain (Fig. 1a). The coordination geometry around Co(II) is distorted trigonal prismatic consisting of CoN_2O_4 chromophore. Cobalt(II) is coordinated to two bridging bidentate terephthalate ligands and one bidentate 2,2′-bipy ligand. One trigonal face is composed of O14 and O24 oxygen atoms of two opposing terephthalate ligands and the N8 atom of the 2,2′-bipy ligand. The second face is composed of O13 and O23 atoms from two terephthalate ligands and N2 atom of the same 2,2′-bipy ligand. The angle between the planes of the two trigonal faces O14O24N8 and O13O23N2 is 9.33°. This deviates from 0°, which is the expected ideal angle for trigonal prismatic geometry.

2 forms a coordination 1D zigzag chain owing to bridging by terephthalate ligands. The zigzag chains form π–π interactions with opposing alternating chains through the rings of the 2,2′-bipy ligands (Fig. 1b) and form a porous grid structure (Fig. 1c). The pores comprise 29.4% of the unit cell volume (619.43 $Å^3$). The centroid–centroid separation between the two opposing rings is 3.738 Å. The opposing 2,2′-bipy ligands are perfectly parallel. The interplanar distance and angle are 3.450 Å and 0°, respectively. The atom–atom distances between the 2,2′-bipy rings are 3.805, 3.878, 3.669, 3.798, 3.688, and 3.621 Å, indicating strong π–π interactions.

3.3 Synthesis of the cobalt–carbon silica nanocomposite ($CoC@SiO_2$)

Upon pyrolysis of cobalt complex **1**, anthracene was added in 1 : 1 weight ratio as an additional bulk carbon source to increase the carbon yield and carbon to cobalt ratio. Furthermore, because it has adjacent aromatic rings, it can be considered to be graphene segments, which increases the chance of obtaining highly graphitized carbon nanostructures. Silica particles were also added in 1 : 1 complex : silica weight ratio. The suggested mechanism involves dissociation of the carbon precursors, deposition of carbon on the silica surface, and filling of the pores. The silica template can be removed

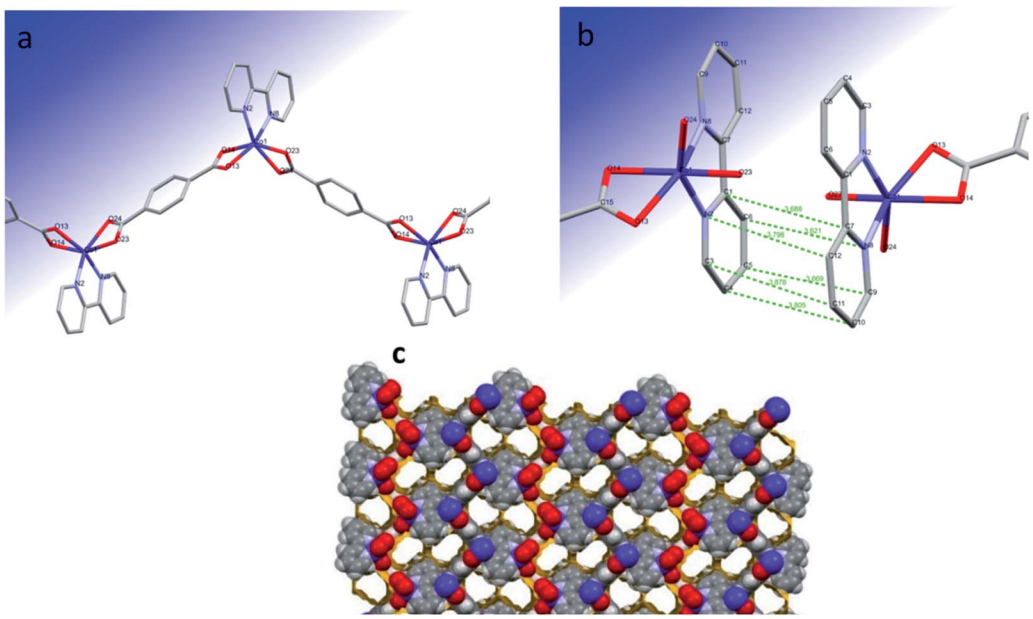

Fig. 1 (a) Zigzag chain structure of the trigonal prismatic complex Co(μ-tph)(2,2′-bipy) (**2**), (b) π–π interaction and (c) 3D network with pores of complex **2**.

using NaOH or HF solution.[29] However, removing the silica support may cause structural changes or collapse of the carbon structures during template dissolution.[30] Therefore, the cobalt–carbon nanostructure was used without post-treatment.

3.4 Characterization of CoC@SiO_2

3.4.1 Morphological structure. Pyrolysis of Co(tph)(2,2′-bipy)·$4H_2O$ (**1**), anthracene, and silica at 600 °C gave CoC@SiO_2-600 (**4**), which consisted of nanostructured sponge-like carbon decorated with cobalt nanoparticles of diameter less than 200 nm, SEM image (Fig. 2a and b). A large portion of the nanoparticles had diameter less than 30 nm and a few particles had diameter of approximately 200 nm. A TEM image of **4** showed cobalt nanoparticles with diameters in the range 10–50 embedded in graphitized carbon (Fig. 2c). Increasing the pyrolysis temperature to 850 °C gave CoC@SiO_2-850 (**3**), which had a different morphology from **4**. SEM images of **3** showed a rough surface containing cobalt nanoparticles with diameters of about 100 nm (Fig. 2d). Furthermore, encapsulated cobalt species with a wide range of diameters were clearly observed using a STEM detector (Fig. 2e). A TEM image of **3** showed graphitized carbon on the surface of a silica particle (Fig. 2f), indicating that the silica particles acted as a supportive substrate that enhanced carbon growth. It is worth mentioning that some randomly curved CNTs with different lengths were also observed in the TEM image of **3**. The proposed mechanism suggests that these CNTs freely and randomly grow out of the zero-state cobalt nanoparticles reduced during pyrolysis.

The change in the type of nitrogen donor ligand or its combination with terephthalic ligand make difference in the structure of cobalt complex. Pyrolysis of complex provide cobalt nanoparticles, the "graphitization catalyst" which in turn determine the morphology of nanocarbon. The morphology of cobalt nanocarbon **3** is affected by the structure of catalyst precursor, the metal–organic framework cobalt complex **1**. The structure of complex MOF with empty pores will results in porous nanocarbon of high surface area for better adsorption, catalytic and electrical property. Thus, the change in starting materials can improve the performance of these nano-composites by studying the morphology of product and correlating it to adsorption performance. In other word, there should be a noticeable correlation between the preparation procedure (starting materials and heating temperature), structure of nano, and the capacity of adsorption. This is in order to optimize the experiment for better performance of nanocarbon as adsorbent. It is noteworthy to mention that the support used also affects the morphology and functional groups of the nanocarbon. Here we have used polar silica, while in another preliminary study we have used the less polar graphite as support and found that the morphology of nanocomposite product has changed.

3.4.2 Raman spectroscopy. In the Raman spectra of **3** and **4** (Fig. 3), two characteristic bands were observed in the first-order region (1100–1800 cm^{-1}), which are called the G band and D band. The D band is characteristic of sp^3 disordered or defect carbon, whereas the G band is characteristic of ordered sp^2 hybridized carbon,[31] indicating the graphitic nature of carbon.

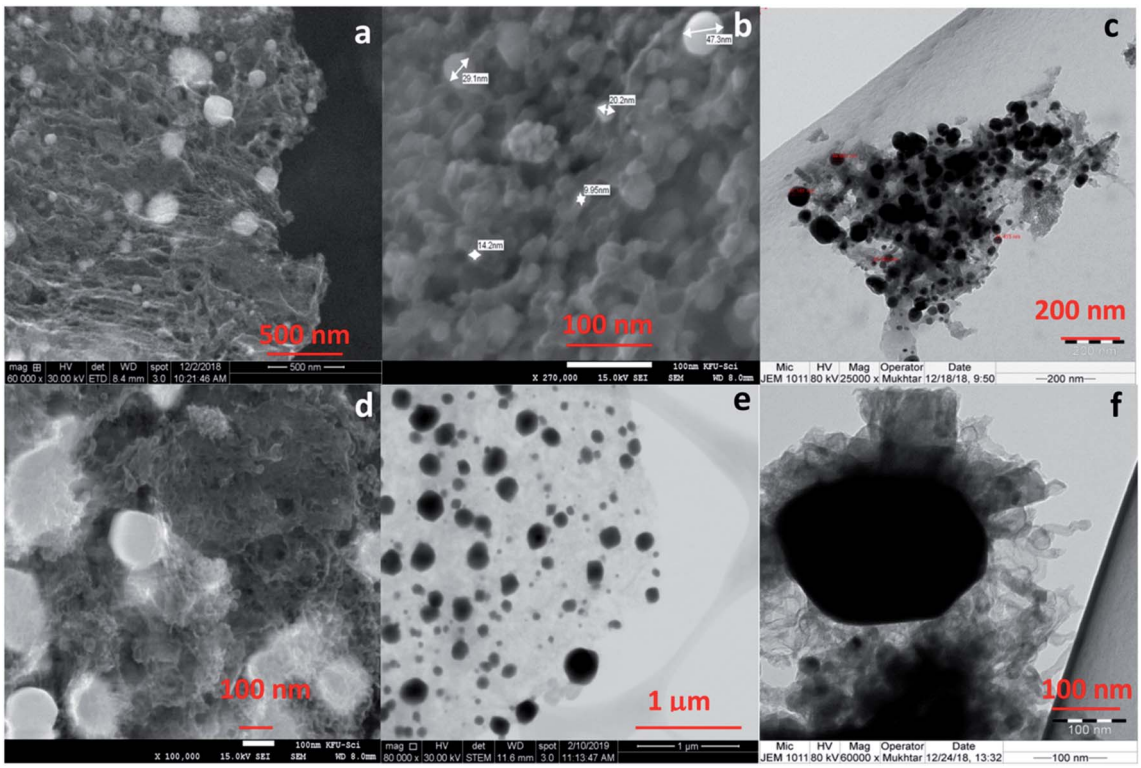

Fig. 2 SEM images of CoC@SiO_2-600 (**4**) (a and b), TEM image of CoC@SiO_2-600 (**4**) (c), SEM images of CoC@SiO_2-850 (**3**) (d and e) and TEM image of CoC@SiO_2-850 (**3**) (f).

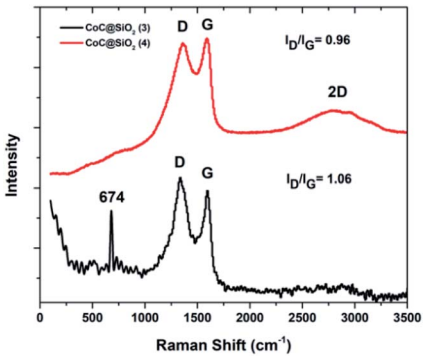

Fig. 3 Raman spectra of CoC@SiO_2-850 (**3**) and CoC@SiO_2-600 (**4**).

Usually, the G band in pure graphite appears at ~1580 cm^{-1}.[32] **3** and **4** showed G bands at higher frequencies of 1600 and 1590 cm^{-1}, respectively. The 10–20 cm^{-1} upshift could be because of different factors, such as defects,[33] strain,[34] doping,[35] and number of layers.[36,37] The D band for both **3** and **4** was at about 1350 cm^{-1}, which agrees with the reported D band of disordered carbon.[32]

The ratio of disordered to graphitic carbon can be represented by the ratio of their corresponding intensities I_D/I_G, which is commonly used as a measure of the degree of graphitization.[38] The I_D/I_G ratio for **4** was = 0.9, whereas that for **3** was 1.07 with a well-separated sharp G band. The third characteristic peak of graphite and graphene is known as the 2D band, which appears in the second-order region. Its width and shape are highly dependent on the stacking order of the graphene sheets along the *c* axis and the number of layers.[39–41]

3 showed a broad 2D band at about 2750 cm^{-1} with relatively low intensity owing to the large number of graphene layers,[37] suggesting that **3** had more graphene layers than **4**. In addition, an extra sharp peak was observed at 674 cm^{-1} in the Raman spectrum of **3**, which is characteristic of the A_{1g} mode of cobalt monoxide (CoO).[42]

3.4.3 XPS. To investigate the chemical compositions and binding states of carbon, oxygen and cobalt, XPS was performed. The XPS survey and high-resolution N 1s, C 1s, Co $2p_{3/2}$, and O 1s spectra of **3** and **4** are shown in Fig. 4 and 5 respectively. The XPS survey confirmed the existence of carbon, cobalt, and oxygen. The high-resolution C 1s XPS spectrum was deconvoluted into four individual curves. In the high-resolution C 1s spectrum, the curve assigned to C–C appeared at 284.6 eV (red curve).[43] In the C 1s spectrum of **3**, the three signals at about 285, 286, and 289 eV were attributed to C–O,[44] C=O, and COOH on the material surface.[45,46] In the C 1s XPS spectrum of **4**, the two peaks corresponding to C–O and C=O appeared at 286.03 and 288.2 eV. The shift to higher energy can be attributed to nitrogen doping, because incorporation of nitrogen into graphitic carbon results in disordering of the graphene lattice.[47,48] For **4**, the peak corresponding to the carboxylic acid group was centred at 289.93 eV.[49] Furthermore, the peak positions obtained by deconvolution of the O 1s spectra confirmed that different oxygen species were present on the carbon surfaces. The peak located at 531.18 eV in the O 1s spectrum of **3**

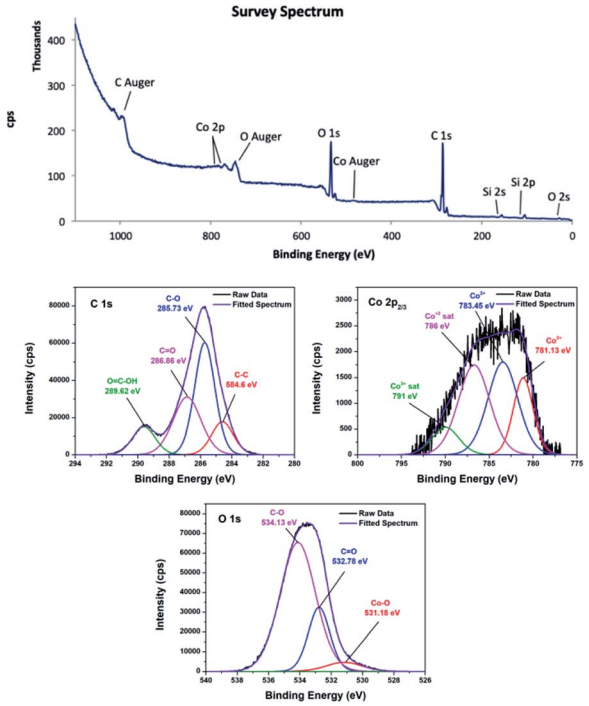

Fig. 4 XPS survey of CoC@SiO_2-850 (**3**), C 1s, O 1s and Co $2p_{3/2}$ spectra.

was attributed to the Co–O bond or hydroxyl group,[50,51] while the peak located at 531.84 eV in the O 1s spectrum of **4** was residual oxygen functional groups.[52] The peaks centred at 532.78 and

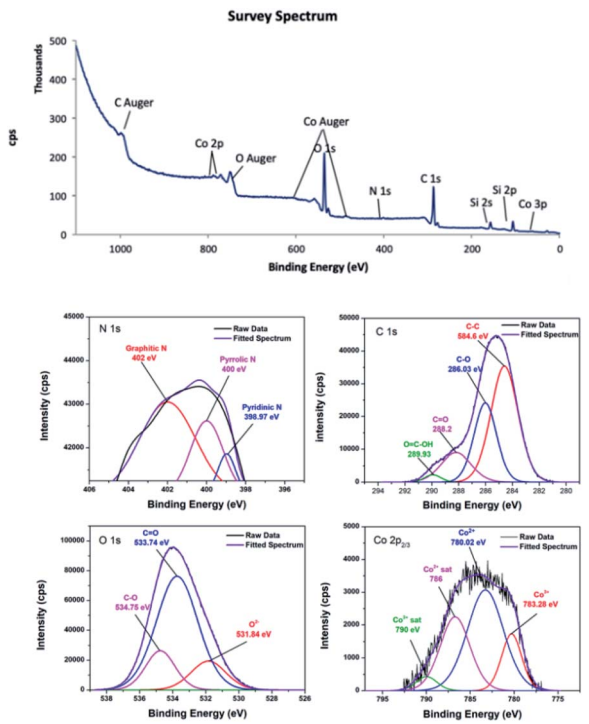

Fig. 5 XPS survey of CoC@SiO_2-850 (**4**), C 1s, O 1s and Co $2p_{3/2}$ spectra.

534.13 eV in the O 1s spectrum of **3** were attributed to C=O and C–O groups, respectively.[53,54] These peaks shifted to higher energies of 533.74 and 534.75 eV in the O 1s spectrum of **4**. In addition, the deconvoluted Co $2p_{3/2}$ spectra confirmed the oxidation states of the cobalt species. Although Co^{2+} and Co^{3+} appear at similar binding energies, they can be distinguishable when Co_3O_4 is present.[55] It is noticeable that **3** and **4** contained a mixture of Co^{2+} and Co^{3+}. In the Co $2p_{3/2}$ XPS spectrum of **3**, the Co^{3+} peak was observed at about 781.13 eV accompanied by a relatively weak satellite peak at about 790.0 eV,[56] whereas the Co^{3+} peak was at about 780.02 eV for 4.[57] The peak at about 783.45 eV was attributed to Co^{2+}.[58] The XPS survey spectrum of **4** showed a trace amount of nitrogen, confirming successful nitrogen doping. The nature of nitrogen can be deduced from the deconvoluted N 1s spectrum. The deconvoluted spectrum showed peaks at 398.9, 400, and 401.81 eV, which were attributed to pyridinic, pyrrolic, and graphitic nitrogen, respectively.[59–61]

The atomic% of carbon calculated from the peak intensities are 70% and 55.7% for **3** and **4**, respectively. In contrast, **3** has relatively lower oxygen content (29.6%) than **4** (43.5%), assuming that pyrolysis temperature should be sufficiently high in order to obtain nanocomposite with high carbon content. In addition, the Co^{2+}/Co^{3+} in **3** is 3.18 and 1.82 in **4**. It can be concluded that Co^{2+}/Co^{3+} is highly sensitive toward pyrolysis temperature.

3.4.4 XRD. To obtain further insight into the chemical environment and to overcome the limitations of XPS in detecting internal species, XRD was performed. The XRD patterns of **3** and **4** are shown in Fig. 6. The XRD patterns confirmed the existence of cobalt in the metallic state, indicating that during pyrolysis cobalt ions were reduced to cobalt crystallites with zero oxidation state, which catalysed graphitization of gaseous carbon from the decomposed organic ligands and additional carbon source. For **3**, only the cubic phase β-Co was detected, which agrees with the fact that β-Co is thermodynamically more stable than hexagonal phase α-Co at high temperature.[62] In contrast, **4** contains a mixture of α-Co and β-Co. The average crystal size of the metallic cobalt nanoparticles was calculated by the Scherrer equation:

$$\tau = \frac{0.9\lambda}{\beta \cos \theta} \quad (1)$$

where τ is the average particle size, λ is the X-ray wavelength, β is the full width at half maximum, and θ is the diffraction angle. The average crystal sizes of α-Co and β-Co metallic cobalt particles for **3** were about 27 and 26 nm, respectively, whereas cobalt particles encapsulated in **4** was about 28 nm.

3.4.5 Surface area and porosity. The nitrogen adsorption/desorption isotherms of **3** and **5** are shown in Fig. 7. The cobalt–carbon/silica nanocomposite **5** was prepared by HCl treatment of **4**. The isotherms were type IV[63] with visible hysteresis loops, which are associated with capillary condensation phenomena of mesoporous materials.[64,65] The isotherm showed rapid adsorption in the low pressure region. This characteristic feature is associated with pores of molecular dimensions,[66] suggesting that **5** contained micropores for rapid adsorption of nitrogen, whose molecular diameter is about 0.364 nm in the ultra-low-pressure region.[66] The nitrogen uptake gradually increased followed by a plateau at about 620 mmHg. At the end of the plateau, a slight increase occurred at about 735 mmHg with an adsorption capacity of 377.97 $cm^3\ g^{-1}$ and a Brunauer–Emmett–Teller (BET) surface area of 335.396 $m^2\ g^{-1}$. This suggests that **5** is an ideal candidate for adsorption of small-molecule gases by van der Waals interactions. The amount of CO_2 adsorbed by **5** was 167.850 $cm^3\ g^{-1}$ (Fig. 7).

3 exhibited gradual nitrogen uptake for $P < 450$, and then the uptake rapidly increased, resulting in nitrogen uptake of 50.95 $cm^3\ g^{-1}$ at 743.9 mmHg. In addition, the hysteresis loop was significantly broader than that of **5**, suggesting a different pore shape because the capillary condensation mechanism is highly dependent on the pore structure of mesoporous materials.[64] The surface areas, pore volumes, and pore sizes of **3** and **5** are given in Table S3.† The surface areas of **5** calculated by the BET, single point, and Barrett–Joyner–Halenda (BJH) methods were significantly greater than those of **3**, and the pore size of the pyrolytic product increased with increasing pyrolysis temperature.

3.5 Adsorption of CV to CoC@SiO_2-850 (3)

3.5.1 Effect of dye initial concentration. The effect of the initial CV concentration on the amount of CV adsorbed to CoC@SiO_2-850 (**3**) from aqueous solution is shown in Fig. S3.† The adsorbed amount of CV increased with increasing initial CV concentration. This is attributed to the high contact probability between the carbon nanostructures and CV molecules. At low CV concentration, the molecules are independently located on

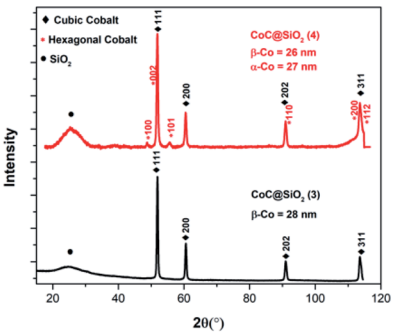

Fig. 6 XRD patterns of CoC@SiO_2-850 (**3**) and CoC@SiO_2-600 (**4**).

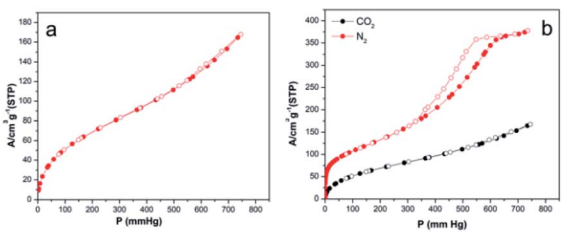

Fig. 7 Nitrogen adsorption/desorption isotherm of **3** (a), nitrogen adsorption/desorption and carbon dioxide adsorption/desorption isotherms of **5** (b).

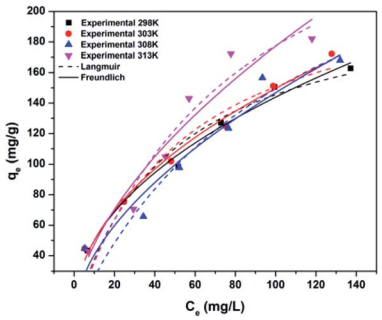

Fig. 8 Freundlich and Langmuir non-linear fits of adsorption of CV to CoC@SiO_2-850 (**3**) at different temperatures.

the outer surface of the adsorbent. With increasing CV concentration, the molecules enter into the interior structure, resulting in higher amount of CV removed.[67] In addition, the percentage removal was very high at low concentration because of the high availability of vacant adsorption sites for CV ion binding. With increasing initial CV concentration, the percentage removal dramatically decreased and then gradually decreased owing to gradual occupation of the binding sites.[68]

3.5.2 Effect of temperature. The adsorption capacity showed an increasing trend with increasing temperature (Fig. 8), indicating the endothermic nature of the adsorption process. This can be attributed to increasing mobility of the CV molecules with increasing temperature. Mobility increases the probability of interaction between the CV molecules and adsorption sites.[69] Another explanation is that the density of the adsorbent decreases with increasing temperature, providing larger pores which facilitate diffusion of CV molecules.[70]

3.5.3 Adsorption isotherm. A wide variety of isotherm models have been developed to obtain insight into the adsorption process.[71] The Langmuir[72–74] and Freundlich[72,74,75] isotherms are the most common isotherms used to fit the experimental data of the liquid/solid adsorption process.

To choose the best isotherm model to represent CV adsorption, the experimental data obtained at different temperatures after achieving equilibrium (24 h contact time) were fitted to the Langmuir and Freundlich isotherm models by non-linear (Fig. 8) and linear regression. The correlation coefficient (R^2), Chi^2, and sum of the squared error (SSE) values were used to determine the best isotherm for the experimental data.

Adsorption of CV followed the Freundlich model better than the Langmuir model because of the higher correlation coefficient and lower Chi^2 and SSE values for the Freundlich model than for the Langmuir model (Table 1). The agreement of the experimental data with the Freundlich isotherm suggested that the adsorbed CV cations formed a multilayer on the surface of **3**.

3.5.4 Adsorption kinetics. The adsorption kinetics describe the rate at which the solute adsorbs on the surface of the adsorbent, and hence the required residence time of the adsorbate can be predicted. Furthermore, investigation of the adsorption kinetics of water pollutants is important to obtain insight into the adsorption mechanism, which ultimately aids in designing suitable water treatment plants.[76] Two kinetic models were applied to describe the adsorption process: the pseudo-first-order and pseudo-second-order kinetics models.[77–80] To investigate which one of the kinetics models best fits the data, R^2 is widely used as an indicator of the agreement between the experimental and calculated data. The values of rate constant for the first-order (k_1), the second-order (k_2) and R^2 are obtained from the linear and non-linear plots at 298 K.[77–80] It is found that R^2 for pseudo-second-order model are 0.9978 and 0.8984, which are higher than that for pseudo-first-order (0.9139, 0.7878) using linear and non-linear regression, respectively. As a result, adsorption of CV to **3** was fitted well by the pseudo-second-order model. This means that the adsorption capacity can be increased by increasing the concentration of the adsorbate and/or the amount of the adsorbent in the adsorbate–adsorbent mixture. k_2 calculated for the second-order model using linear and non-linear regressions are 0.000436 (g mg^{-1} min^{-1}) and 0.000468 (g mg^{-1} min^{-1}), respectively. Unlikely, k_1 values are 0.00656 (min^{-1}) and 0.0287 (min^{-1}). The significant difference in the k_1 values could be attributed to the fact that adsorption process obeys the second-order model rather than the first-order kinetic.

3.5.5 Adsorption mechanism. Since the newly prepared adsorbent contains graphitic (aromatic rings) and oxygenated functional group. It is expected to be efficient for the removal of aromatic dyes with polar groups, the criterion for selecting the target dye depend on the structure of dyes present in the wastewater. It is proposed that the presence of aromatic graphite and oxygen-containing functional groups in the prepared nanocomposites can create new adsorption sites for dyes with polar functional groups and aromatic rings by making hydrogen bonds and π–π interaction respectively. Therefore, three different dyes with aromatic rings and amine groups which belong to three different classes were selected; cationic triarylmethane dye (CV), cationic heterocyclic dye belongs to thi-azine class (MB) and anionic azo dye (MO).

Upon treatment of 10 mL of dye with an initial concentration of 100 ppm with 0.04 g of **3** for 24 h at 25 °C, the % removal of CV (98.3%) was little higher than that of MB (96.6%) and MO (88.3%) (Fig. S4†). The prepared cobalt nanocarbon acted efficiently as adsorbent for these three dyes. But the focus in this paper was only on crystal violet.

Interestingly, **3** showed almost equal capacities for anionic and cationic dyes, suggesting that π–π interaction between the aromatic rings of the dye and nanocarbon plays a major role in the adsorption process.

An in-depth understanding of adsorption mechanism aids in determining the rate-limiting step, which in turn aids in optimizing the adsorption conditions.[81] The rate-controlling step can be film diffusion, where the adsorbate passes through the boundary layer to the external surface of the adsorbent particles, and/or intra-particle diffusion, where adsorbate molecules move into the interior of the adsorbent particles.[82]

The Weber–Morris intra-particle diffusion equation is widely used to determine if intra-particle diffusion is the rate-controlling step.[79]

$$q_t = K_i t^{1/2} + C_i \quad (2)$$

Table 1 Langmuir and Freundlich isotherm parameters for adsorption of CV to 3

	Langmuir			Freundlich		
	Parameter	Linear	Non-linear	Parameter	Linear	Non-linear
298 K	q_{max} (mg g^{-1})	202.02	214.16	K_F (mg g^{-1}) (L mg^{-1})$^{1/n}$	18.33	17.30
	K_L (L mg^{-1})	0.0261	0.0212	n	2.2430	2.1736
	R^2	0.9446	0.9363	R^2	0.9892	0.9835
	Chi^2	0.9776	133.49	Chi^2	0.9956	34.55
	SSE	0.0132	533.98	SSE	0.0107	138.19
	R_L	0.1131	0.0035			
303 K	q_{max} (mg g^{-1})	206.61	230.23	K_F (mg g^{-1}) (L mg^{-1})$^{1/n}$	21.02	16.74
	K_L (L mg^{-1})	0.0269	0.0189	n	2.3774	2.1026
	R^2	0.9128	0.9076	R^2	0.9819	0.9847
	Chi^2	0.9645	208.52	Chi^2	0.9927	34.37
	SSE	0.0187	834.09	SSE	0.0179	137.49
	R_L	0.1101	0.1495			
308 K	q_{max} (mg g^{-1})	225.22	314.31	K_F (mg g^{-1}) (L mg^{-1})$^{1/n}$	19.55	11.16
	K_L (L mg^{-1})	0.0186	0.0090	n	2.3558	1.7868
	R^2	0.7535	0.8745	R^2	0.8744	0.9201
	Chi^2	0.8960	303.33	Chi^2	0.9484	193.2101
	SSE	0.0489	1213.32	SSE	0.1343	772.8405
	R_L	0.1515	0.2687			
313 K	q_{max} (mg g^{-1})	278.55	321.18	K_F (mg g^{-1}) (L mg^{-1})$^{1/n}$	12.93	12.61
	K_L (L mg^{-1})	0.0163	0.01235	n	1.7701	1.7427
	R^2	0.7892	0.9204	R^2	0.9308	0.9125
	Chi^2	0.9118	250.32	Chi^2	0.9719	275.30
	SSE	0.0196	1001.28	SSE	0.0888	1101.20
	R_L	0.1692	0.2125			

where K_i (mg g^{-1} min$^{-1/2}$) is the intra-particle diffusion rate constant for stage i, C_i (mg g^{-1}) is the adsorption constant, and q_t (mg g^{-1}) is the amount of solute adsorbed at time t (min). The resistance to external mass transfer increases as the intercept increases.[79,83–85]

Applying the Weber–Morris intra-particle diffusion equation resulted in a double linear plot, suggesting that the adsorption process occurs in two stages before it reaches its equilibrium (Fig. S5†). The first line is attributed to instantaneous or external surface adsorption. The second line is attributed to the intra-particle diffusion stage, where the dye molecules diffuse through the pores of the adsorbent.[86] Adsorption was initially rapid owing to availability of vacant adsorption sites. After 90 min, adsorption slowed down in the second stage owing to fractional occupation of the adsorption sites and blocking of their accessibility. The linear line of the second stage did not pass through the origin. Therefore, intra-particle diffusion was not the only rate-limiting step but other mechanisms were involved.[79] The contribution of surface adsorption to the rate-controlling step can be deduced from the value of C_i because it represents the thickness of the boundary layer. The contribution of surface adsorption to the rate-limiting step is greater for larger C_i value.[76,79] Applying the intra-particle diffusion equation gave $K_i = 0.52907$ mg g^{-1} min$^{-1/2}$ and $C_i = 36.7035$ mg g^{-1} with $R^2 = 0.9080$.

3.5.6 Thermodynamics of adsorption. The thermodynamic parameters are important for predicting the performance and mechanism of adsorption, and hence for optimizing the adsorption process. The ΔH, ΔS, and ΔG values for adsorption of CV dye to **3** calculated from the plot of ln K *versus* $1/T$.[67,87] The positive ΔH value (18.902 kJ mol^{-1}) indicated that the adsorption process was endothermic in nature. This agrees with the isotherm results, where q_{max} increased with increasing temperature (Table 1). The positive ΔS value (66.367 J mol^{-1} K^{-1}) indicated the spontaneous nature of the adsorption process in the temperature range investigated. The increase of the ΔG value with increasing temperature (−0.875 at 298 K, −1.207 at 303 K, −1.539 at 308 K and −1.871 at 313 K) indicated that the adsorption process was more favourable at high temperature.

3.5.7 FTIR spectra of the carbon nanostructures after adsorption. The FTIR spectra of **3** before and after adsorption of CV are shown in Fig. S6.† The two bands assigned to Si–O–Si at 1015 and 779 cm^{-1} remained after adsorption, suggesting that the Si–O–Si group was not involved in the interaction between the adsorbent and adsorbate.[88] After adsorption, two new peaks appeared at 1589 and 1366 cm^{-1}, which were assigned to the C=C stretching vibration of the aromatic ring and the C–N stretching vibration of the aromatic tertiary amine of CV, respectively.[89] Except for the two bands assigned to CV, no new peaks appeared after adsorption, suggesting that the adsorption process occurred by weak bonds, such as π–π stacking of the aromatic rings between CV and the carbon nanostructures.

3.5.8 Column study

3.5.8.1 Breakthrough curves. A breakthrough curve is a plot of the ratio of the solute concentration in the effluent to its concentration in the feed solution (C_e/C_0) against time (min) or effluent volume (mL). A fixed-bed adsorption column was studied in order to investigate the capability, regeneration and recycling efficiency of (**3**) in the continuous adsorption system.

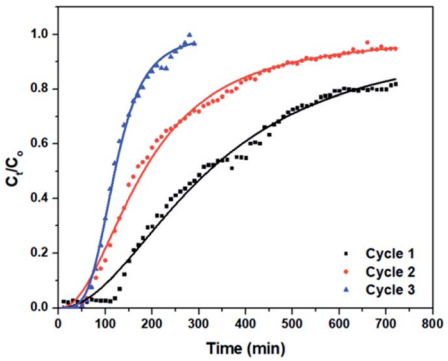

Fig. 9 Yan *et al.* non-linear fit of adsorption of CV using column packed with **3**.

In the desorption process, dilute hydrochloric acid was used as a suitable eluting agent since it is inexpensive and widely used as elution agent for desorbing cationic dyes from adsorbents.

The breakthrough curves for the three cycles of CV adsorption onto (**3**) in the fixed-bed column are shown in Fig. 9. In the first cycle, the breakthrough point was reached after 120 min. In the second and third cycles, the breakthrough point occurred after about 50 min. In addition, it is obvious that the column in the first cycle and the second cycles required more than 720 min to be fully saturated and reach equilibrium, while it required only 290 min in the first cycle. Fig. S7† shows the plot of the concentration of adsorbed amount of CV (C_{ad}), *versus* time (t) for each cycle, from which the area under the breakthrough curve was determined.[90,91] The maximum bed capacity (q_e) is 36.29, 22.85 and 12.30 mg g^{-1} for the first, second and third cycles, respectively, while the percentage removal is 50.40% in the first cycle. It decreased to 42.40% in the third cycle.

The first desorption cycle of **3** required about 200 mL of 0.5 M HCl solution at a flow rate of 1 mL min^{-1}, after which further desorption was negligible. Around 47.3% of the CV species were desorbed in the first cycle and the eluting solution was initially highly concentrated, which leads to easy handling, recovery and reuse of CV. The column bed was then washed with deionized water with continuous measurement of the pH, to ensure the removal of excess H^+ ions from the column. Mineral acids are proton-exchange agents that can extract CV cations from **3**. An excessive amount of H^+ ions can reduce the CV adsorption uptake. Therefore, washing **3** with deionized water can remove H^+ ions and thus **3** can be regenerated for use in further adsorption cycles.

The relatively low efficiency of HCl solution as an elution agent is because of the strongly adsorbed CV, which may require higher concentration of HCl. In addition, this explains the decrease in capacities of the bed column in the second and third cycles.

3.5.8.2 Column kinetic study. Several models can be used to describe the column behaviour, including the Thomas,[92] Yoon–Nelson,[93] and Yan *et al.*[94] models.

The Thomas model assumes that the adsorption process follows Langmuir kinetics of adsorption–desorption with negligible axial dispersion in the column because the rate-driving force follows pseudo-second-order reversible kinetics. The non-linear expression of the Thomas model is

$$\frac{C_e}{C_0} = \frac{1}{1 + e^{\frac{k_T}{Q}(q_T m C_0 V)}} \quad (3)$$

where C_0 is the initial concentration of the feed solution, k_T (mL mg^{-1} min^{-1}) is the Thomas rate constant, q_T (mg g^{-1}) is the Thomas column capacity, m (g) is the amount of adsorbent in the column, and Q (mL min^{-1}) is the volumetric flow rate.[92,95]

The Yoon–Nelson model assumes that the rate of decrease of the probability of adsorption for each adsorbate species is proportional to the probability of adsorbate adsorption and the probability of adsorbate breakthrough on the adsorbent. The non-linear form of the Yoon–Nelson model is

$$\frac{C_e}{C_0} = \frac{1}{1 + e^{k_{YN}(\Gamma - t)}} \quad (4)$$

where k_{YN} (min^{-1}) and Γ (min) are the rate constant and time required for 50% adsorbate breakthrough, respectively. Because the amount of adsorbate adsorbed on the bed is half of the total amount of the adsorbate entering the bed within 2Γ periods, then

$$q_{YN} = \frac{q_{total}}{m} = \frac{\frac{1}{2}C_0\left(\frac{Q}{1000}\right)(2\Gamma)}{m} = \frac{C_0 Q \Gamma}{1000m} \quad (5)$$

where q_{YN} is the Yoon–Nelson column capacity, Q (mL min^{-1}) is the volumetric flow rate, C_0 (mg L^{-1}) is the initial concentration of the feed solution, and m (g) is the total dry mass of the adsorbent in the column.[93,96]

The empirical Yan *et al.*[94] model can overcome the limitations of the Thomas model, especially its inability to predict the effluent concentration with respect to zero time. The non-linear form of the Yan *et al.* model is

$$\frac{C_e}{C_0} = 1 - \frac{1}{1 + \left(\frac{Q^2 t}{k_Y q_Y m}\right)^{\frac{k_Y C_0}{Q}}} \quad (6)$$

where k_Y (L min^{-1} mg^{-1}) is the kinetic rate constant and q_Y (mg g^{-1}) is the maximum Yan column capacity.

Comparing the values of Chi^2, SSE, and R^2 (Table 2), Yan *et al.* model fits the experimental data best with the highest R^2 value and lowest Chi^2 and SSE values (Fig. 9). Thus, the Yan *et al.* model can be used to describe the adsorption behaviour of CV to **3** in the fixed-bed column. The value of correlation coefficients for Thomas and Yoon–Nelson models were lower than that for the Yan *et al.* model under the same experimental conditions, which makes them less applicable. The column capacities obtained by the Thomas and Yoon–Nelson models were 20.66 mg g^{-1}, and that obtained by the Yan *et al.* model was 8.49 mg g^{-1} (Table 2).

3.5.9 Comparison of adsorption capacity of (3) with other nanocarbon adsorbents. The maximum crystal violet adsorption capacities of various nanocarbon sorbent were compared with the capacity of cobalt–carbon/silica nanocomposites CoC@SiO_2-850 (**3**), in Table 3. The comparison indicates that (**3**) has higher adsorption capacity of CV than other modified graphene oxide and Zr–C composite adsorbent. It is less than the

Table 2 Column kinetic parameters for removal of CV by (3)

Thomas		Yoon–Nelson		Yan *et al.*	
Cycle 1					
k_T (mL min^{-1} mg^{-1})	0.1279	k_{YN} (min^{-1})	0.0064	k_Y (mL min^{-1} mg^{-1})	0.04031
q_T (mg g^{-1})	35.80	q_{YN} (mg g^{-1})	35.80	q_Y (mg g^{-1})	15.88
		τ (min)	358.09		
R^2	0.9408	R^2	0.9408	R^2	0.9891
Chi^2	0.00467	Chi^2	0.00467	Chi^2	0.00085
SSE	0.3270	SSE	0.3270	SSE	0.06018
Cycle 2					
k_T (mL min^{-1} mg^{-1})	0.207	k_{YN} (min^{-1})	0.01039	k_Y (mL min^{-1} mg^{-1})	0.04279
q_T (mg g^{-1})	20.66	q_{YN} (mg g^{-1})	20.66	q_Y (mg g^{-1})	8.49
		τ (min)	206.65		
R^2	0.94403	R^2	0.9440	R^2	0.9945
Chi^2	0.00518	Chi^2	0.00518	Chi^2	0.00051
SSE	0.3627	SSE	0.36267	SSE	0.03589
Cycle 3					
k_T (mL (min^{-1} mg^{-1}))	0.645	k_{YN} (min^{-1})	0.03229	k_Y (mL (min^{-1} mg^{-1}))	0.07775
q_T (mg g^{-1})	12.53	q_{YN} (mg g^{-1})	12.52	q_Y (mg g^{-1})	3.09
		τ (min)	125.29		
R^2	0.9805	R^2	0.9805	R^2	0.9964
Chi^2	0.00282	Chi^2	0.00282	Chi^2	0.00051
SSE	0.07605	SSE	0.07605	SSE	0.01397

Table 3 Comparison of crystal violet adsorption capacity of CoC@SiO_2-850 (3) with other nanocarbon adsorbents

Adsorbent	Capacity (mg g^{-1})	Reference
Fe_3O_4/graphene/ biochar composite	436.68	17
MWCNTs-OH	988	18
MWCNTs-COOH	1275	18
EDTA/graphene oxide functionalized corncob	95.87	19
Zirconia/carbon composite	243	20
Grafted sodium alginate/ ZnO/graphene oxide composite	13.85	21
CoC@SiO_2-850 (3)	321.18	This study

more expensive modified graphene and MWCNT. However, (3) has the advantage of being prepared in a simple, high yield and cheap method. The substrate silica was used as 1/3 of the starting materials, is abundant and cheap. The durability of (3) because of silica support causes (3) to be easily packed into column for industrial application in water treatment.

4. Conclusion

1D zigzag chain of new polymeric structure of the porous MOF Co(μ-tph)(2,2′ bipy) (2) was successfully synthesized and the crystal structure was confirmed by single-crystal X-ray. The 1D chains are stacked in alternating fashion along "*a*" axis through π–π interactions to form a 3D supramolecular network. In addition, CoC@SiO_2 nanocomposites with interesting morphologies were also successfully synthesized by solid-state pyrolysis of a mixture of the mixed-ligand complex Co(tph)(2,2′-bipy)·$4H_2O$ (1), anthracene and silica. Based on SEM and TEM, pyrolysis at 600 °C gave CoC@SiO_2-600 (4) with sponge-like cobalt–carbon nanostructures, while pyrolysis at 850 °C gave CoC@SiO_2-850 (3) with a rough surface decorated with pointing cobalt species and CNTs, suggesting that the morphology of nanocarbon, size and shape of the cobalt species are highly dependent on the pyrolysis temperature. Furthermore, XPS revealed that the carbon nanostructures were functionalized with different oxygen-containing functional groups, including carboxylic acid group. In addition, the presence of metallic cobalt nanoparticles embedded within the graphitized carbon was confirmed by XRD. The efficiency of (3) for removal of CV from aqueous solution was also investigated. The Langmuir adsorption capacity was 214 mg g^{-1}. It was found that the adsorption process best fitted Freundlich isotherm and pseudo-second-order kinetic model. In addition, thermodynamic study, showed that the adsorption process was endothermic and entropically favourable. In addition, ΔG values indicated that the adsorption process was spontaneous and more favourable at higher temperature. Furthermore, fixed-bed column study showed that the adsorption capacity was 36.29 mg g^{-1} and that Yan *et al.* model adequately described the continuous adsorption process.

Conflicts of interest

There are no conflicts to declare.

Acknowledgements

The authors acknowledge the Deanship of Scientific Research at King Faisal University for the financial support under Annual Research Project (Grant No. 180101). Prof. Michael Zaworotko,

University of Limerick, is acknowledged for his contribution to gas adsorption analysis.

References

1 V. K. Gupta, *J. Environ. Manage.*, 2009, **90**, 2313–2342.
2 E. Forgacsa, T. Cserháti and G. Orosb, *Environ. Int.*, 2004, **30**, 953–971.
3 H. S. Rai, M. S. Bhattacharyya, J. Singh, T. K. Bansal, P. Vats and U. C. Banerjee, *Crit. Rev. Environ. Sci. Technol.*, 2005, **35**, 219–238.
4 A. K. Mishra, T. Arockiadoss and S. Ramaprabhu, *Chem. Eng. J.*, 2010, **162**, 1026–1034.
5 Y.-H. Li, J. Ding, Z. Luan, Z. Di, Y. Zhu, C. Xu, D. Wu and B. Wei, *Carbon*, 2003, **41**, 2787–2792.
6 C. Chen, J. Hu, D. Xu, X. Tan, Y. Meng and X. Wang, *J. Colloid Interface Sci.*, 2008, **323**, 33–41.
7 M. Endo, K. Takeuchi, S. Igarashi, K. Kobori, M. Shiraishi and H. W. Kroto, *J. Phys. Chem. Solids*, 1993, **54**, 1841–1848.
8 S. Iijima, *Nature*, 1991, **354**, 56–58.
9 T. Guo, P. Nikolaev, A. Thess, D. T. Colbert and R. E. Smalley, *Chem. Phys. Lett.*, 1995, **243**, 49–54.
10 P. I. Dosa, C. Erben, V. S. Iyer, K. P. C. Vollhardt and I. M. Wasser, *J. Am. Chem. Soc.*, 1999, **121**, 10430–10431.
11 S. Rondeau-Gagné and J.-F. Morin, *Chem. Soc. Rev.*, 2014, **43**, 85–98.
12 L. Tang, Y. Cai, G. Yang, Y. Liu, G. Zeng, Y. Zhou, S. Li, J. Wang, S. Zhang, Y. Fang and Y. He, *Appl. Surf. Sci.*, 2014, **314**, 746–753.
13 Y. Pang, G. Zeng, L. Tang, Y. Zhang, Y. Liu, X. Lei, Z. Li, J. Zhang and G. Xie, *Desalination*, 2011, **281**, 278–284.
14 T. Phenrat, Y. Liu, R. D. Tilton and G. V. Lowry, *Environ. Sci. Technol.*, 2009, **43**, 1507–1514.
15 C. Jiao, Y. Wang, M. Li, Q. Wu, C. Wang and Z. Wang, *J. Magn. Magn. Mater.*, 2016, **407**, 24–30.
16 H. H. Hammud, B. El Hamaoui, N. H. Noubani, X. Feng, Z.-S. Wu, K. Mullen and K. Ayub, *Nanosci. Nanotechnol.–Asia*, 2018, **8**, 263–280.
17 C. Du, Y. Song, S. Shi, B. Jiang, J. Yang and S. Xiao, *Sci. Total Environ.*, 2020, **711**, 134662.
18 L. Sellaoui, G. L. Dotto, E. C. Peres, Y. Benguerba, É. C. Lima, A. Ben Lamine and A. Erto, *J. Mol. Liq.*, 2017, **248**, 890–897.
19 H. Wang, X. Lai, W. Zhao, Y. Chen, X. Yang, X. Meng and Y. Li, *RSC Adv.*, 2019, **9**, 21996–22003.
20 Z. Hasan, D.-W. Cho, I.-H. Nam, C.-M. Chon and H. Song, *Materials*, 2016, **9**, 261.
21 S. K. Mohamed, S. H. Hegazy, N. A. Abdelwahab and A. M. Ramadan, *Int. J. Biol. Macromol.*, 2018, **108**, 1185–1198.
22 Y. Park, D.-S. Shin, S. H. Woo, N. S. Choi, K. H. Shin, S. M. Oh, K. T. Lee and S. Y. Hong, *Adv. Mater.*, 2012, **24**, 3562–3567.
23 J. Rogan, D. Poleti, L. Karanović, G. Bogdanović, A. Spasojević-De Biré and D. M. Petrović, *Polyhedron*, 2000, **19**, 1415–1421.
24 N. Preda, L. Mihut, M. Baibarac, I. Baltog, M. Husanu, C. Bucur and T. Velula, *Rom. J. Phys.*, 2009, **54**, 667–675.
25 H. T. Varghese, C. Y. Panicker, D. Philip, K. Sreevalsan and V. Anithakumary, *Spectrochim. Acta, Part A*, 2007, **68**, 817–822.
26 C. A. Téllez S, E. Hollauer, M. Mondragon and V. M. Castaño, *Spectrochim. Acta, Part A*, 2001, **57**, 993–1007, DOI: 10.1016/S1386-1425(00)00428-5.
27 M. Nara, H. Torii and M. Tasumi, *J. Phys. Chem.*, 1996, **100**, 19735–20174.
28 R. J. Acheson and A. K. Galwey, *J. Chem. Soc. A*, 1967, 1174–1178.
29 J. Liu, N. P. Wickramaratne, S. Z. Qiao and M. Jaroniec, *Nat. Mater.*, 2015, **14**, 763–774.
30 L. Lafi, D. Cossement and R. Chahine, *Carbon*, 2005, **43**, 1347–1357, DOI: 10.1016/j.carbon.2004.12.032.
31 X. Liu, B. Frank, W. Zhang, T. P. Cotter, R. Schlögl and D. S. Su, *Angew. Chem., Int. Ed.*, 2011, **50**, 3318–3322.
32 M. B. Vázquez-Santos, E. Geissler, K. László, J.-N. Rouzaud, A. Martínez-Alonso and J. M. D. Tascón, *J. Phys. Chem. C*, 2012, **116**, 257–268.
33 A. Das, B. Chakraborty and A. K. Sood, *Bull. Mater. Sci.*, 2008, **31**, 579–584.
34 X. Duan, H. Son, B. Gao, J. Zhang, T. Wu, G. G. Samsonidze, M. S. Dresselhaus, Z. Liu and J. Kong, *Nano Lett.*, 2007, **7**, 2116–2121.
35 A. Das, S. Pisana, B. Chakraborty, S. Piscanec, S. K. Saha, U. V Waghmare, K. S. Novoselov, H. R. Krishnamurthy, A. K. Geim, A. C. Ferrari and A. K. Sood, *Nat. Nanotechnol.*, 2008, **3**, 210–215.
36 D. Graf, F. Molitor, K. Ensslin, C. Stampfer, A. Jungen, C. Hierold and L. Wirtz, *Nano Lett.*, 2007, **7**, 238–242.
37 D. Wei, Y. Liu, Y. Wang, H. Zhang, L. Huang and G. Yu, *Nano Lett.*, 2009, **9**, 1752–1758.
38 G. Yuan, X. Li, Z. Dong, A. Westwood and B. Rand, *Carbon*, 2013, **68**, 426–439.
39 A. C. Ferrari, J. C. Meyer, V. Scardaci, C. Casiraghi, M. Lazzeri, F. Mauri, S. Piscanec, D. Jiang, K. S. Novoselov, S. Roth and A. K. Geim, *Phys. Rev. Lett.*, 2006, **97**, 187401.
40 A. Gupta, G. Chen, P. Joshi, S. Tadigadapa and P. C. Eklund, *Nano Lett.*, 2006, **6**, 2667–2673.
41 M. A. Pimenta, G. Dresselhaus, M. S. Dresselhaus, L. G. Cançado, A. Jorio and R. Saito, *Phys. Chem. Chem. Phys.*, 2007, **9**, 1276–1290.
42 N. Sanpo, C. C. Berndt, A. S. M. Ang and J. Wang, *Surf. Coat. Technol.*, 2013, **232**, 247–253.
43 Y. Huang, Y. Gao, Q. Zhang, Y. Zhang, J. Cao, W. Ho and S. C. Lee, *J. Hazard. Mater.*, 2018, **354**, 54–62.
44 Y. Zhu, J. Cui, S. An, Z. Li, Y. Zhang and W. He, *J. Alloys Compd.*, 2019, **810**, 151932.
45 S. Indrawirawan, H. Sun, X. Duan and S. Wang, *Appl. Catal., B*, 2015, **179**, 352–362.
46 M. B. Ahmed, J. L. Zhou, H. H. Ngo, W. Guo, A. H. Johir, K. Sornalingam, D. Belhaj and M. Kallel, *Chem. Eng. J.*, 2017, **322**, 571–581.
47 Z. Mou, X. Chen, Y. Du, X. Wang, P. Yang and S. Wang, *Appl. Surf. Sci.*, 2011, **258**, 1704–1710.

48 R. Droppa Jr, P. Hammer, A. C. M. Carvalho, M. C. Dos Santos and F. Alvarez, *J. Non-Cryst. Solids*, 2002, **299**, 874–879.
49 K. Tadyszak, K. Chybczyńska, P. Ławniczak, A. Zalewska, B. Cieniek, M. Gonet and M. Murias, *J. Magn. Magn. Mater.*, 2019, **492**, 165656.
50 Y. Ge, K. Kan, Y. Yang, L. Zhou, L. Jing, P. Shen, L. Li and K. Shi, *J. Mater. Chem. A*, 2014, **2**, 4961–4969, DOI: 10.1039/c3ta14607c.
51 H. Wang, C. Qing, J. Guo, A. A. Aref, D. Sun, B. Wang and Y. Tang, *J. Mater. Chem. A*, 2014, **2**, 11776–11783.
52 G. Bharath, R. Madhu, S.-M. Chen, V. Veeramani, D. Mangalaraj and N. Ponpandian, *J. Mater. Chem. A*, 2015, **3**, 15529–15539.
53 M. M. Aghayan, *Appl. Organomet. Chem.*, 2019, **33**, 1–11.
54 X. Miao, D. Qu, D. Yang, B. Nie, Y. Zhao and H. Fan, *Adv. Mater.*, 2018, **30**, 1704740.
55 A. Gabe, J. García-Aguilar, Á. Berenguer-Murcia, E. Morallón and D. Cazorla-Amorós, *Appl. Catal., B*, 2017, **217**, 303–312.
56 P. W. Menezes, A. Indra, D. González-Flores, N. R. Sahraie, I. Zaharieva, M. Schwarze, P. Strasser, H. Dau and M. Driess, *ACS Catal.*, 2015, **5**, 2017–2027.
57 K. J. Kim, J. H. Lee, T. Y. Koh and M. H. Kim, *Electrochim. Acta*, 2016, **200**, 84–89.
58 X. Zhang, J. Zhao, Z. Song, H. Zhao and W. Liu, *ChemistrySelect*, 2019, **4**, 8902–8909.
59 Y. Liu, Z. Jin, J. Wang, R. Cui, H. Sun, F. Peng, L. Wei, Z. Wang, X. Liang and L. Peng, *Adv. Funct. Mater.*, 2011, **21**, 986–992.
60 T. Susi, T. Pichler and P. Ayala, *Beilstein J. Nanotechnol.*, 2015, **6**, 177–192.
61 T. Schiros, D. Nordlund, L. Pálová, D. Prezzi, L. Zhao, K. S. Kim, U. Wurstbauer, C. Gutiérrez, D. Delongchamp and C. Jaye, *Nano Lett.*, 2012, **12**, 4025–4031.
62 J. Sort, J. Nogués, S. Suriñach, J. S. Muñoz and M. D. Baró, *Mater. Sci. Eng., A*, 2004, **375–377**, 869–873.
63 K. S. W. Sing, *Pure Appl. Chem.*, 1985, **57**(4), 603–619.
64 S. J. Gregg and K. S. W. Sing, *Adsorption Surface Area and Porosity*, Academic Press, London, 2nd edn, 1982.
65 S. Dantas, K. C. Struckhoff, M. Thommes and A. V. Neimark, *Langmuir*, 2019, **35**, 11291–11298.
66 Q. Yang, P. Hou, S. Bai, M. Wang and H. Cheng, *Chem. Phys. Lett.*, 2001, **345**, 18–24.
67 Z. Liu and F. S. Zhang, *J. Hazard. Mater.*, 2009, **167**, 933–939.
68 S. K. Low, M. C. Tan and N. L. Chin, *Ultrason. Sonochem.*, 2018, **48**, 64–70.
69 J. Fu, Z. Chen, M. Wang, S. Liu, J. Zhang, J. Zhang, R. Han and Q. Xu, *Chem. Eng. J.*, 2015, **259**, 53–61.
70 M. S. Chiou and H. Y. Li, *Chemosphere*, 2003, **50**, 1095–1105.
71 A. S. Negi and S. C. Anand, *Textbook of Physical Chemistry*, New Age International, New Delhi, 1985.
72 I. Langmuir, *J. Am. Chem. Soc.*, 1917, **39**, 1848–1906.
73 T. W. Weber and R. K. Chakravorti, *AIChE J.*, 1974, **20**, 228–238.
74 K. Y. Foo and B. H. Hameed, *Chem. Eng. J.*, 2010, **156**, 2–10.
75 H. M. F. Freundlich, *J. Phys. Chem.*, 1906, **57**, 385–471.
76 A. Gürses, Ç. Doğar, M. Yalçin, M. Açikyildiz, R. Bayrak and S. Karaca, *J. Hazard. Mater.*, 2006, **131**, 217–228.
77 S. K. Lagergren, *K. Sven. Vetenskapsakad. Handl.*, 1898, **24**, 1–39.
78 W. Rudzinski and W. Plazinski, *J. Phys. Chem. B*, 2006, **110**, 16514–16525.
79 M. A. Ahmad and R. Alrozi, *Chem. Eng. J.*, 2011, **171**, 510–516.
80 Y.-S. Ho and G. McKay, *Water Res.*, 2000, **34**, 735–742.
81 H. K. Boparai, M. Joseph and D. M. O'Carroll, *J. Hazard. Mater.*, 2011, **186**, 458–465.
82 E. Worch, *Adsorption Technology in Water Treatment: Fundamentals, Processes, and Modeling*, Walter de Gruyter GmbH, Dresden, 2012.
83 I. A. W. Tan, A. L. Ahmad and B. H. Hameed, *J. Hazard. Mater.*, 2009, **164**, 473–482.
84 B. H. Hameed and M. I. El-Khaiary, *J. Hazard. Mater.*, 2008, **154**, 639–648.
85 A. A. Lewinsky, *Hazardous Materials and Wastewater: Treatment, Removal and Analysis*, Nova Science Publishers, New York, 2007.
86 Q. Huang, X. Lin, L. Xiong, C. Huang, H. Zhang, M. Luo, L. Tian and X. Chen, *RSC Adv.*, 2017, **7**, 23896–23906.
87 P. W. Atkins, *Physical Chemistry*, Oxford University Press, London, 4th edn, 1990.
88 J. Serra, P. González, S. Liste, C. Serra, S. Chiussi, B. León, M. Pérez-Amor, H. O. Ylänen and M. Hupa, *J. Non-Cryst. Solids*, 2003, **332**, 20–27.
89 J. Cheriaa, M. Khaireddine, M. Rouabhia and A. Bakhrouf, *Sci. World J.*, 2012, **2012**, 512454.
90 B. Sivasankar, *Engineering Chemistry*, Tata McGraw-Hill Education, New Delhi, 2008.
91 S. H. Hasan, D. Ranjan and M. Talat, *J. Hazard. Mater.*, 2010, **181**, 1134–1142.
92 H. C. Thomas, *J. Am. Chem. Soc.*, 1944, **66**, 1664–1666.
93 Y. H. Yoon and J. H. Nelson, *Am. Ind. Hyg. Assoc. J.*, 1984, **45**, 509–516.
94 G. Yan, T. Viraraghavan and M. Chen, *Adsorpt. Sci. Technol.*, 2001, **19**, 25–43.
95 Z. Aksu and F. Gönen, *Process Biochem.*, 2004, **39**, 599–613.
96 J. Qu, Y. Li, T. Zang, Y. Jin, X. Liu and L. Yan, *Environ. Eng. Sci.*, 2019, **36**, 1162–1169.